

Stratigraphy and paleogeographic reconstruction of the Doushantuo Formation

The Ediacaran Doushantuo Formation (ca. 635–551 Ma)¹ in South China overlies the late Cryogenian Nantuo Formation (ca. 654–635 Ma)². The type section of the Doushantuo Formation is defined in the Yangtze Gorges area where it is divided into four members^{3–6}. Member I refers to the 3–6-m-thick cap carbonate at the base of the Doushantuo Formation. Member II consists of alternating organic-rich shale and carbonates with abundant centimeter-scale chert nodules. Member III consists of predominately carbonates with bedded chert layers and minor shale laminae. Member IV refers to the ca. 10-m-thick black, organic-rich shale interval at the top of the Doushantuo Formation. The thickness of the Doushantuo Formation varies from 40 to 200 m and lateral facies change from shallow-water phosphatic dolostone to deeper-water black shale and siliceous shales^{4–6}. The Doushantuo cap carbonate (Member I)^{7,8} and the organic-rich black shale of Member IV serve as the marker beds for the overall stratigraphic correlation across the Nanhua basin⁶.

The Doushantuo Formation was deposited as part of a passive continental margin succession^{9–11}. The paleogeographic reconstruction^{9–11} of the Doushantuo Formation (Fig. S1) was based on the facies analyses across the shelf-to-basin transects⁶. The uniform thickness and similar facies of the Doushantuo cap carbonate (Member I) and its immediately overlying black shales (lower Member II) across the basin suggest an open shelf setting at the beginning of the Doushantuo deposition (Fig. S1a). The open shelf evolved into a rimmed shelf (Fig. S1b) after the Doushantuo cap carbonate deposition, from a topographic high inherited from the Nantuo glaciation and/or through preferential carbonate growth at the shelf margin⁶. This change is marked by the presence of shallow-water carbonate facies with exposure features in the shelf

margin and by the abundance of olistostrome carbonates and slump blocks in the upper slope sections adjacent to the open ocean side of the platform margin (Fig. S1b)⁶.

Most of the existing geochemical studies of the Doushantuo Formation have been focused on the Yangtze Gorges or adjacent areas (e.g., ref. 3, 12, 13). Existing redox sensitive element (RSE) analyses of the lower Doushantuo Formation from this area^{12,13} did not reveal high RSE enrichments or a signal for a large fractionation of microbial sulphate reduction indicative of high (> 1 mM) dissolved sulphate concentrations. Unusually low RSE values from this region have been ascribed to basin isolation from the open ocean¹³. Alternative interpretation of the low RSE values from the Yangtze Gorges area could be oxic-dysoxic water column conditions that did not capture the ocean dissolved RSE concentration and that sulphate reduction was restricted to porewaters (closed system behavior). This study focuses on deep-water sections in the open-ocean side of the Yangtze platform (Fig. S1).

Sequence stratigraphic interpretation of the lower Doushantuo Formation

The 3–6-m-thick Doushantuo cap carbonate is the most widespread and distinctive stratigraphic unit across the Nanhua basin^{6–8}. The cap carbonate has a sharp contact with the underlying glacial diamictite of the Nantuo Formation, with no interbedded carbonate and diamictite at the transition. Instead, in most studied sections across the basin, there is an 8–20-cm thick claystone/siltstone layer separating the cap carbonate and diamictite^{2,8}. These features suggest that the Doushantuo cap carbonate was deposited during the late stage of postglacial transgression when continental ice sheets have largely disappeared in the Yangtze block^{2,8}. Diachronous cap carbonate deposition tracking glacioeustatic flooding, reported from the Keilberg cap dolostone in Namibia¹⁴ and the Nuccaleena Formation in Australia¹⁵, is not present

in the Doushantuo cap carbonate and may have happened earlier, likely during the deposition of the Nantuo Formation^{2,8}. Given the transitional facies change from the cap carbonate to its overlying black shales¹⁶, the deglacial isostatic rebound may have also happened before cap carbonate deposition, although it has been argued that the ‘dissolution’ features and barites atop the cap carbonate in some shelf sections may record ice-melting isostatic rebound¹⁷.

The basal Member II black shales have a transitional contact with the underlying cap carbonate across the basin^{8,16} and were most likely deposited during latest transgression or early highstand of sea level. Subsequent sea-level fall formed exposure surfaces at the platform margin and slump blocks and olistostrome carbonates in the upper slope environments^{4,6,18}, but these features are stratigraphically higher than our sampled intervals. The black shales are thinly laminated, without wave- or storm-generated coarse-grained beds¹⁶, suggesting their deposition well below the storm wave base.

Sample location, paleobathymetric estimation, and age constraints

The lower Doushantuo Formation black shales were collected from recently excavated outcrop sections. Samples were collected at an average spacing of 20 cm and, for the present work, samples with macroscopic pyrites were avoided.

Three sections were chosen to cover the upper slope to basinal paleo-depositional environments⁶ (Fig. S1): (1) the upper slope section in Taoying, Guizhou province (27°50′01.5″N, 109°01′03.9″E), (2) the lower slope section in Wuhe, Guizhou province (26°45′93.6″N, 108°25′00.5″E), and (3) the basinal section in Yuanjia, Hunan province (27°29′23″N, E110°14′37.4″E).

Based on the basin reconstruction, the cap carbonate and the basal Member II shales were deposited from a passive continental margin that inherited the topographic gradient from the Cryogenian continental margin^{6,8,11}. Paleobathymetric estimation based on the continental slope gradient¹¹ and accommodation space inferred from the thickness of Cambrian–early Silurian stratigraphic units (backstripping analyses)^{8,10} suggest that the water depth of the basinal section (Yuanjia; section 3) were greater than ~1000 m.

Our samples cover the first 5–9-m-thick black shales above the Doushantuo cap carbonate (or 9.5 m to 13.7 m above the base of the Doushantuo Formation; Table S1). We estimated that the age of the sampled interval is likely between ca. 635 Ma and 630 Ma (or conservatively, no younger than ca. 614 Ma), based on the following evidence: (1) The Doushantuo cap carbonate has been dated in the Yangtze Gorges area (shelf section) as 635.2 ± 0.6 Ma¹. This age was from an ash bed 2.3 m above the base of the Doushantuo Formation (within the cap carbonate). From an adjacent section in the same area, an ash bed 5 m above the Doushantuo cap carbonate (9.5 m above the base of the Doushantuo Formation) was dated as 632.5 ± 0.5 Ma¹. Hence, the duration of the 7.2-m-thick strata at the lower Doushantuo Formation in the Yangtze Gorges area is ~3 Myr. Assuming approximately synchronous deposition of the distinctive cap carbonate member and its immediate overlying black shale during the late transgression and early highstand, the sampled intervals (9.5–13.7 m thick) could be > 635 Ma and < 630 Ma. (2) The sampled interval is within the depositional sequence associated with the postglacial transgression⁶. Olistostrome carbonates and slump blocks indicative of sea-level fall are found in slope sections, but they are above the sampled intervals. (3) Samples are within the carbon isotope excursion associated with the cap carbonate and its overlying strata¹⁶. (4) The overall thickness of the Doushantuo Formation in measured sections,

constrained by two marker beds (the cap carbonate and Member IV organic-rich black shales), is consistent with the stratigraphic correlation that the basal Member II in slope–basinal sections may be time-equivalent with that in the Yangtze Gorges area⁶. For example, the thickness of the Doushantuo Formation in the Yangtze Gorges area is 155 m thick, and in the Wuhe section (loc. 2; Fig. S1) it is 120 m thick. In the Yangtze Gorges area, an age of 614 ± 7.6 Ma was obtained from the middle Doushantuo Formation¹⁹, at a stratigraphic position much higher than the basal member II shales. Thus, even with a conservative estimation, the analyzed basal member II shales should be older than ca. 614 Ma. In summary, litho-, sequence and chemostratigraphic correlation of the well-dated cap carbonate and its overlying shale interval (in the Yangtze Gorges area) across the basin suggest that the age of our analyzed shales is likely ca. 635–630 Ma, but any U-Pb zircon ages and/or Re-Os ages from the basinal sections could provide additional support for this age assignment.

Notes on the Cryogenian–early Ediacaran paleontological record

Historically, the prevailing view was that metazoans first appeared during the early Ediacaran Period^{3,20–22}, shortly after the termination of the late Cryogenian (Marinoan) ‘Snowball Earth’ glaciation (ca. 635 Ma). However, recent molecular clock estimates place the origin of crown-group animals in the Cryogenian period, but these animals, if they existed, were likely detritus feeders with minimum oxygen requirements²³. There are sponge-biomarkers²⁴ and claims of sponge-like fossils in Cryogenian or older rocks^{25–27}, but some of these fossils are controversial²⁸. Again, even if they are correctly interpreted, Cryogenian animals are likely simple metazoans with very limited oxygen demand²⁹.

Animal embryo-like fossils from the early-middle Ediacaran Doushantuo Formation^{20,21} have been challenged³⁰, but existing evidence seem to support that they more likely represent

stem-group metazoans^{31,32}. The Lantian biota contains an assemblage of morphologically differentiated macrofossils²²; some of them can be reasonably interpreted as non-poriferan metazoans²². Further, there is a radiation in marine algae following the Marinoan glaciation, which has been linked to shift in ecosystem complexity driven by metazoan increase in trophic levels^{33,34}. In the modern ocean, algae morphology is driven by metazoan grazing pressure rather than light or nutrient demands³⁵. Therefore, it is likely that the appearance of novel morphologies in primary producers, after a billion year period of sluggish evolutionary innovation, is linked to a major change in ecosystem structure³³. Thus, there is evidence for significant biological innovation in the earliest Ediacaran.

It is important, however, to note that although metazoans certainly had evolved and diversified in the early Ediacaran, animals with energetically expensive and oxygen-demanding lifestyles (e.g., locomotion, carnivory, burrowing) appeared much later in the fossil record (< 590–558 Ma)^{36–38}—more than 40 million years after pervasive early Ediacaran (ca. 635–630 Ma) ocean oxygenation documented in our work. Ocean ventilation could have certainly set the stage for early animals and their subsequent evolution, but it is not necessarily the direct trigger for bilaterian radiation.

Analytical methods

Major and trace elemental abundances, iron speciation, and total organic carbon (TOC) were analyzed at the W. M. Keck Foundation Laboratory for Environmental Biogeochemistry, Arizona State University (ASU) and at the Biogeochemistry lab at the University of California, Riverside (UCR), following previously published methods^{39–42}. Powdered sample splits were ashed for 8–10 hours at 550°C and dissolved completely by HF-HNO₃-HCL acid digestion³⁹.

Trace and major element concentrations were determined on a ThermoFinnigan X-Series (ASU) and Agilent 7500E (UCR) quadrupole ICP-MS (inductively coupled plasma mass spectrometry). Accuracy and precision were monitored with duplicate samples and the US Geological Survey Devonian black shale standard SDO-1, and reproducibility in individual runs was better than 95% for the presented elements. Iron speciation analyses were conducted at UCR, following published methods¹². Biogeochemically highly reactive iron (Fe_{HR}) is defined as pyrite iron (Fe_{pyrite}) plus other iron phases that are potentially reactive with hydrogen sulphide on diagenetic time scales: carbonate-associated iron (Fe_{Carb}), ferric oxides (Fe_{Ox}), and magnetite (Fe_{Mag}). Hence highly reactive iron $Fe_{HR} = Fe_{pyrite} + Fe_{Carb} + Fe_{Ox} + Fe_{Mag}$ (ref. 42). Fe_{pyrite} was calculated (assuming a stoichiometry of FeS_2) from the weight percentage of sulphur extracted during a 2 hour hot chromous chloride distillation followed by iodometric titration⁴⁰⁻⁴². Acid-volatile sulphide (AVS) extraction is also used to determine pyrite stoichiometry, which indicates that the iron sulphides in the Doushantuo shales are predominantly pyrites. Other iron species including Fe_{Carb} , Fe_{Ox} , and Fe_{Mag} were extracted sequentially⁴² using sodium acetate solution (for Fe_{Carb}), dithionite solution (for Fe_{Ox}), and ammonium oxalate (Fe_{Mag}). The sequential extracts were analyzed with an Agilent 7500ce ICP-MS. As mentioned above, total iron concentrations (Fe_T) were determined by HF-HNO₃-HCl acid digestion followed by ICP-MS analysis. Reproducibility of iron measurements, monitored by duplicate analyses within and between sample batches, was better than 94%. Total organic carbon (TOC) contents were determined by taking the difference between carbonate carbon liberated by 4M HCl and total carbon released by combustion at 1,400°C, both of which were measured with an ELTRA C/S determinator at UCR⁴¹. Lastly, also at UCR, pyrite-S was extracted for isotope measurements using the same

chromous chloride distillation but in this case, reprecipitating the pyrite-S as Ag_2S . Sulphur isotope measurements were made with a ThermoFinnigan Delta V continuous-flow stable-isotope-ratio mass spectrometer. Sulphur isotope data are reported as per mil (‰) deviations from the isotope composition of Vienna Cañon Diablo Troilite (VCDT). Reproducibility was better than 0.2% on the basis of single-run and long-term standard monitoring.

Trace elements as a redox tracer of ocean oxygenation

Redox sensitive elements (RSE) (e.g. Mo, V, and U) can be used as a tracer of the Earth's oxygenation^{41,43}. They have minimum detrital influence relative to enrichments in anoxic settings⁴⁴ and their enrichments in modern anoxic shales, in first order, scale with their dissolved concentration in seawater^{45,46}. However, when applying RSE redox proxies to black shales of the geological successions, the following conditions need to be considered:

- (1) Because RSEs are conservative (Mo and U) or quasi-conservative (V) under oxic conditions, their enrichments in shales deposited under oxic water column are commonly low and close to their crustal values (except for sediments very rich in Fe-Mn oxyhydroxides)^{44,47-49}. Thus 'oxic' or 'suboxic' shales do not effectively capture the high dissolved RSE concentrations in modern seawater.
- (2) The high dissolved RSE concentrations in modern seawater are most effectively captured in shales deposited in anoxic basins. The long resident times of Mo (800–440 kyrs)^{47,50}, V (~50 kyrs)⁴⁷, and U (250-500 kyrs)⁴⁷ relative to the ocean mixing time (~1-1.5 kyrs) warrant that Mo, V, and U in anoxic basins, even with some restricted access to the open ocean, track the global average RSE concentration. However, strong basin restriction (isolation) without open ocean seawater renewal would deplete water column RSE concentrations and result in low RSE enrichments in anoxic shales^{45,46}. For example, in

the Black Sea, the bottom water column Mo concentration is only 2-3% of the open ocean and the Mo/TOC values in black shales drop to 4.5 ± 1 , compared to the Mo/TOC values of 25 ± 5 in shales of the Cariaco Basin, where water column Mo concentration is 70–85% of the open ocean^{45,46}.

- (3) RSE removal in suboxic environments is more efficient than oxic environments but at least one order of magnitude less effective compared to anoxic environments⁴⁶. Thus shales deposited in suboxic environments may have variable RSE enrichments between crustal values and the low end of anoxic shale values^{47,51,52}. In addition, because Mo, V, and U behave differently in suboxic environments, their enrichments in a particular ‘suboxic’ shale bed are not necessarily correlatable⁴⁷⁻⁴⁹.

In the modern oxygenated ocean, only anoxic shales in marine basins with access to the open ocean effectively capture the high dissolved RSE concentration in seawater. When applying to the ancient record, high RSE enrichments comparable to those of the modern anoxic shales provide definitive evidence for high dissolved RSE in an oxygenated ocean; there is no other alternative sedimentary process to enrich RSEs to such high values. However, low RSE values from a particular stratigraphic unit would have much less definitive meaning. It could be resulted from strong basin restriction (isolation) in an oxygenated ocean (comparable to the Black Sea), low RSE enrichments in oxic/suboxic local environments (comparable to modern oxic/suboxic sediments), or low dissolved RSE concentrations in poorly oxygenated ocean. When RSE enrichments from a particular stratigraphic unit are low, it can be used to infer a less oxygenated ocean only when paleogeographic reconstruction and other geochemical and/or paleontological evidence exclude strong basin restriction, and independent geochemical data indicate persistent anoxia/euxinia⁴¹.

Iron speciation and redox fluctuations

One of the intriguing findings is that the lower Doushantuo Formation black shales has submeter-scale variations in Fe_{HR}/Fe_T and Fe_{pyrite}/Fe_{HR} ratios (Fig. S2; Table S1). Post-depositional alteration (e.g., through weathering and oxic fluid interaction) could potentially result in changes in iron speciation, but very low iron oxides in most samples (Table S2; Fig. S2) exclude this possibility. Sudden increase in sedimentation rate (e.g., gravity flow) may dilute highly reactive iron contents, resulting in low Fe_{HR}/Fe_T values^{53,54}. However, field and petrographic observations did not find any coarse-grained layers or obvious turbidites, which would be indicative of rapid deposition within the lower Doushantuo black shales. Thus, it is likely that the submeter-scale variations in Fe_{HR}/Fe_T and Fe_{pyrite}/Fe_{HR} recorded dynamic redox fluctuations characterized by alternating oxic, suboxic, and anoxic local environments.

Overall the Fe_T contents of the lower Doushantuo black shales increase from the shelf¹² and upper slope sections towards the lower slope and basin sections (Table S1), consistent with Fe redox cycling and transportation towards deeper water environments⁵⁴. However, a large portion of the Doushantuo samples have unusually low Fe_T/Al ratios (< 0.1 ; Table S1), much lower than the average crustal value of 0.5 (refs 55, 56). The origin of such low Fe_T/Al ratios from the Doushantuo Formation in this study and from previous reports^{12,13} is not well understood and the details remain as an ongoing task to investigate. However, these deviations from typical shales suggest that the Doushantuo black shales are not equivalent to average continental margin shales and sediments in which iron proxies are calibrated. Therefore, Fe speciation results (Fig. S2) should be viewed with caution. For instance, it may not be possible to use Fe_{HR}/Fe_T ratios of the Doushantuo black shales to delineate anoxia given deviations from typical continental margin major element chemistry. For this reason, we do not use Fe_{HR}/Fe_T

ratios as a quantitative paleoredox proxy in this study. However, $\text{Fe}_{\text{pyrite}}/\text{Fe}_{\text{HR}}$ ratios will still be a reliable gauge for the sulphide availability in the depositional environment.

Temporal Mo, V, U variations and redox fluctuations

Similar to the temporal variations in iron speciation, large variability in redox-sensitive element (RSE) enrichments has been observed in lower Doushantuo Formation black shales (Table S1; Fig. 2). Intervals with high Mo, V, and U enrichments are often adjacent (< 0.2 m) to intervals with near crustal, un-enriched values. Combined petrographic and geochemical evidence strongly suggest that variability in RSE enrichments within the lower Doushantuo Formation are linked to depositional processes. For instance, sulphides in examined samples, based on petrographic and SEM-EDS (Scanning Electron Microscope-Energy Dispersive Spectroscopy) analyses, are present largely as framboidal or finely disseminated pyrites, which point towards minimal post-depositional sulphide alteration. Within sections of the Doushantuo Formation there are mm-thick laminae with macroscopic pyrites¹⁶, but such intervals have been carefully avoided in our sample preparation. With very limited exceptions, the shales were devoid of hematite, which could be indicative of oxic weathering or supergene alteration (Table S1). Further, acid-volatile sulphide (AVS) extraction indicates that the iron sulphides in the Doushantuo shales are predominantly pyrites. Processes that would alter RSE enrichments would also alter sulphides. Thus, the preservation of early diagenetic sulphide textures suggests that the shales host marine RSE signatures. The Phanerozoic-like RSE enrichments and the variability in enrichments are consistent with the presence of a globally well-oxygenated ocean but dynamic local redox conditions.

The drop of RSE enrichments after the basal Doushantuo Formation shales

In the basal Doushantuo Formation shales there is an apparent drop of Mo (Mo/TOC), V(V/TOC), and U(U/TOC) values after the first few meters (Table S1 and Fig. 2 in main text). While the high RSE enrichments at the basal interval unequivocally require a large oceanic RSE reservoir in response to a well-oxygenated ocean–atmosphere system, low RSE values are much less definitive and could be derived from (1) strong basin restriction, (2) shift to less reducing, local environments, or (3) a decrease in the size of oceanic RSE reservoir.

Strong basin restriction (isolation) is a least likely option. Existing tectonic and paleogeographic reconstructions^{6,10,57,58} do not attach South China to the interior or margin of another major continent, and the low pyrite sulphur isotopes imply ready availability of sulphate in basinal waters, most likely in direct contact with the global ocean.

The most cautious interpretation for the drop of RSE enrichments is a local shift to less reducing environments on the basis of the following evidence and reasoning: (1) The sub-meter scale fluctuations in RSE enrichments at the basal few meters were unlikely caused by rapid contractions and expansion of marine RSE reservoirs. (2) Despite high RSE enrichments at the basal interval in slope-basin sections, coeval basal Doushantuo Formation shales from the shelf sections^{12,13} did not have high RSE enrichments (despite that Fe proxies, given traditional interpretations, point toward anoxic conditions). The lack of high RSE enrichments in the shelf sections^{12,13} is best explained by ineffective uptake of RSEs in less reducing (e.g., oxic-suboxic) environments rather than recording small oceanic RSE reservoirs. (3) The lack of RSE enrichments in shelf sections is consistent with our reasoning that the Fe speciation data from the Doushantuo Formation should be taken with caution. Because of the unusually low total Fe (see Table S1 and ref. 12, 13) from the Doushantuo black shales in general, high Fe_{HR}/Fe_T (> 0.38) with low Fe_{pyrite}/Fe_{HR} (< 0.8) values indicative of ferruginous conditions may record oxic

conditions, while high $\text{Fe}_{\text{HR}}/\text{Fe}_{\text{T}}$ (> 0.38) with high $\text{Fe}_{\text{pyrite}}/\text{Fe}_{\text{HR}}$ (> 0.8) values could potentially record sulphidic conditions in porewaters.

The third interpretation, i.e., the drop of RSE enrichments after the basal Doushantuo shales records the shrink of the oceanic RSE reservoirs, is the most intriguing. It implies that the early Ediacaran oxygenation was not a unidirectional process. However, the drop of RSE enrichments down to near crustal values requires a shift back to reducing ocean conditions typical of mid-Proterozoic and Archean oceans^{41,43}. This seems to be difficult in light of the trace metal biolimitation stabilizing feedback^{41,59} and overall increasing biodiversity in early-middle Ediacaran^{23,33}. However, given the scarcity of data from the Ediacaran successions, a comprehensive test in broader paleogeographic settings of the Nanhua basin and in other global successions is warranted.

Molybdenum and Vanadium mass balance model

Overview of the modern Mo cycle

In the modern ocean, Mo has a residence time of ~440–800 thousand years and an average seawater concentration of 105 nM^{47,50}. Mo is enriched in sediments by adsorption onto organic matter under reducing conditions^{45,46}, or by redox cycling of Mn-Fe-oxyhydroxides⁴⁹. In the modern oxygenated ocean, molybdenum (Mo) is present as Mo (VI) in the form of molybdate (MoO_4^{2-})⁴⁹. Under reducing and sulphidic conditions, Mo is present in the form of Mo (IV) and often present as thiomolybdate (MoOxS_{4-x})⁴⁹. Conversion of molybdate to particle reactive thiomolybdate requires the presence of free sulphide. Helz and others⁶⁰ recently proposed that Mo is removed into anoxic settings as Fe-Mo(IV)-S particles, which may also be

scavenged by sinking organic matter. However, this mineral phase has not been identified in any natural setting.

Oxic, suboxic and euxinic environments are important burial sinks for Mo, but their burial rates are markedly different from each other^{47,49-52}. Oxic marine sediments tend to have low crustal average (1-2 ppm), if not measuring ferromanganese oxides, where molybdate ions are adsorbed onto ferromanganese rich crusts^{49,51}. Mo can be removed faster (~10 times the crustal average) under suboxic environment, where mild reducing conditions (sulphidic pore waters) prevail below sediment-water interface^{46,61}. Mo burial in sediments deposited under an anoxic water column is typically several orders of magnitude higher than in suboxic sediments. Although the removal mechanisms are slightly different in each individual setting, the modern oceanic Mo budget is balanced by oxic, suboxic and euxinic settings, which collectively constitute ~35%, ~50% and ~15% of the total riverine flux of Mo into the ocean^{41,47}. The modern Mo cycle is assumed to be in steady state.

Overview of the modern V cycle

In the modern ocean, V has a residence time of 50-100 thousand years and an average seawater concentration of 36 nM^{47,48}. In oxic water, vanadium is present as V(V) in the form of vanadate oxyanions (HVO_4^{2-} and HVO_4^-), while in mildly reducing conditions V(V) is reduced to V(IV) and present in the form of vanadyl ions (VO^{2+}) and related hydroxyl species ($\text{VO}(\text{OH})_3^-$) or hydroxides ($\text{VO}(\text{OH})_2$)^{44,47}. In strongly reducing conditions with high dissolved sulphide (H_2S) concentrations, V(IV) will be further reduced to V(III), which may precipitate as V_2O_3 or $\text{V}(\text{OH})_3$ (ref. 44). V(IV) and V(III) can be scavenged by organic matter, leading to V enrichment in sediments deposited under an anoxic water column⁴⁷. Under oxic conditions, similar to Mo, V is only removed in significant quantities associated with Mn and Fe oxides^{44,47,48}. One significant

difference between the Mo and V global mass balances is the ratio of riverine particulate to dissolved flux, which for V (100) is much higher than Mo (2.5)^{47,48}. Another difference is that in mildly reducing (i.e., a subset of ‘suboxic’) conditions, V is diffusively released from sediments. This process is tightly coupled with the redox cycle of Mn⁴⁸. Thus, suboxic seafloor is considered as a source for V but a sink for Mo in mass balance calculations⁴⁸. It is possible that the modern V cycle is not currently fully in steady state and is adjusting from the last glacial maximum⁴⁸. However, for geochemical modeling we have assumed a steady state.

Mass balance equations and time-dependent modeling results

The effects of perturbations to Mo and V geochemical cycles can be estimated using a first order model based on modern element mass balances^{47,48}. We modeled a simple time-dependent sensitivity of seawater concentration of Mo and V to their areal extent of different reducing conditions over time (Fig. S3). Using the modern mass balance of each metal, an instantaneous change is assumed at $t = 0$ using modern seawater source and sink fluxes. The mass balance is controlled by the difference of input and output fluxes of the particular element in the ocean so that:

$$\mathbf{(dC_{(RSE)}/dt)} = \mathbf{F_{source} - F_{sinks}}$$

For the modern Mo cycle:

$$\mathbf{Vo(dC_{(Mo)}/dt)} = \mathbf{Jr - (Aso * Fso) - (Ao * Fo) - (Aex * Fex)}$$

For the modern V cycle:

$$\mathbf{Vo(dC_{(V)}/dt)} = \mathbf{Jr + (Aso * Fso) - (Ao * Fo) - (Aa * Fa) - (Aex * Fex) - Jh}$$

Where, V_o is the volume of the ocean; $C_{(Mo)}$ and $C_{(V)}$ are the concentrations of Mo and V in seawater, respectively. J_r is the riverine flux; A_o is the area of oxic sediments; A_a is the area of anoxic sediments; A_{so} is the area of the suboxic environments (oxic water column with reducing sediments); A_{ex} is the area of euxinic sediments; F_o is the oxic flux; F_a is the anoxic flux; F_{so} is the ‘suboxic’ source flux (see above); and J_h is the hydrothermal burial flux. The equations are solved for time t (ref. 48). Modern mass balances of Mo and V^{47, 48} are summarized as below:

RSE	Riverine Flux	Ocean Concentration	Hydrothermal Flux	Environment	Oxic (O)	Suboxic (SO)	Anoxic (A)	Euxinic (EX)
V	5.4 x 10 ⁸ mol/yr	36 nmol/L	5.5 x 10 ⁸ mol/yr	Seafloor fraction	0.97	0.025	0.003	0.0005
				Burial Rate (nmol/cm ² yr)	0.12	6.1	4.3	38.0
Mo	1.8 x 10 ⁸ mol/yr	105 nmol/L	-	Seafloor fraction	0.9	0.01	-	0.0005
				Burial Rate (nmol/cm ² yr)	0.021	2.61	-	12.51
Seafloor area: (3.5-3.61) x 10 ⁸ km ² , Ocean volume: (1.3-1.37) x 10 ¹⁸ m ³								

The output fluxes are strongly dependent on the redox environment⁴⁷⁻⁴⁹ and therefore we assumed that burial rates (b) in individual sink (i) scale with RSE inventory [Mo]. RSE removal fluxes (F) in each sink are also scaled to their respective seafloor coverage (A)—a first order or direct feedback model:

$$b_i = b_{i(\text{today})} \cdot [\text{Mo}/\text{Mo}_{(\text{today})}]$$

$$F_i = A_i \cdot b_i$$

A simple first order differential equation can be derived as⁴⁸:

$$(dC_{(\text{RSE})}/dt) = \lambda - \gamma \cdot \text{RSE} \quad \text{where } \lambda = F_{\text{source}} \quad \text{and } \gamma = F_{\text{sinks}}$$

For time series, the exponentially derived end concentration (RSE_{term}) after time (t) is given by:

$$RSE_t = RSE_{term} + (RSE_{t=0} - RSE_{term}) \bullet \exp(-\gamma t)$$

$$\text{Where } RSE_{term} = F_{source}/F_{sinks} = (\lambda/\gamma)$$

We modeled the change in seawater concentration of Mo and V through time by (1) increasing the riverine flux of Mo and V with increased weathering, and (2) increasing the extent of anoxic/euxinic environments in the ocean. The results show that doubling the riverine flux of Mo and V can be easily compensated for by a small increase (~2%) in anoxic marine seafloor⁴⁷ (Fig. S3). More importantly, a small areal increase in euxinic seafloor can crash the ocean Mo and V reservoirs on a time scale much shorter than the response time to doubling the riverine flux (Fig. S3). For example, a 2–3% increase in euxinic seafloor would crash the Mo and V reservoirs at a time scale of < 0.5 Myr and 0.04 Myr, for Mo and V respectively. Therefore, we consider that the sudden increase in Mo and V (and other redox sensitive elements such as U) to Phanerozoic levels in the post-cap-carbonate black shales was a result of changes in the ocean oxidation state rather than an increase in the riverine flux. Increased weathering and riverine flux may have played a role during the maximum glacial retreat, prior to the deposition of the Doushantuo Member II black shales, but that alone would not result in long-term (hundred thousand to million year time scale) increase of oceanic Mo and V reservoirs in the postglacial ocean.

Secular trends in sulphur isotopes and Mo, V concentrations

Sulphur isotopes

The lower Doushantuo black shales in the slope and basinal sections have sulphide sulphur isotopes ($\delta^{34}S_{pyrite}$) down to -35‰ (canyon diablo troilite, CDT). Coeval carbonate associated sulphate sulphur isotopes ($\delta^{34}S_{CAS}$) from the shelf sections, including Xiaofenghe⁶²,

Jiulongwan^{3,12}, Zhongling¹², and Weng'an⁶³ sections, vary from +32‰ to +41‰, with an average of +34‰. Assuming that the $\delta^{34}\text{S}_{\text{CAS}}$ data from the shelf sections recorded the seawater sulphate sulphur isotope signature, the maximum sulphate-sulphide sulphur isotope offset ($\Delta^{34}\text{S} = \delta^{34}\text{S}_{\text{CAS}} - \delta^{34}\text{S}_{\text{pyrite}}$) during the deposition of the lower Doushantuo Member II shales in the deep basinal section would be $\geq 65\%$. Such high $\Delta^{34}\text{S}$ values are equivalent to maximum fractionations by sulphate reducing bacteria^{64,65} and the maximum pyrite-coeval sulphate offset observed in the Phanerozoic rock record (Fig. S4)^{43,66,67}. Since increase in the isotopic offset between pyrites and seawater sulphate in the Neoproterozoic has been commonly linked to growth of the marine sulphate reservoir and increase of surface oxidation⁶⁶⁻⁶⁸, the large sulphur isotope fractionation in the basal Member II shales (Fig. S4) is consistent with a well-oxygenated ocean during deposition of the lower Doushantuo Member II shales. Sulphate-sulphide sulphur isotope offset $> 65\%$ are thought to indicate at least 1 mM sulphate⁶⁵ and thus near Phanerozoic levels of sulphate⁶⁶.

Secular Mo, Mo/TOC variations

The secular variations of Mo, Mo/TOC, V, V/TOC through time (Fig. 3 in main text) have been summarized by Scott and others⁴¹ and Och and Shields⁴³. We have added additional data that were not included in previous compilations, including new data for this study from the ca. 640 Ma Black River Dolomite⁶⁹ (Table S3) and the most recently published data from ca. 663 Ma Datangpo Formation⁷⁰ (see references in Table S2). The unusually high ($> 10,000$ ppm) Mo and V concentrations from the lower Cambrian metal-enriched (Ni-Mo-PGE) sulphide deposits in south China (compiled in ref. 43) may be linked to high temperature mineralization rather than seawater derived metal enrichment⁷¹ and therefore, data from this deposit are not included in Figure 3. A complete list of references that were used for the compilation of Mo, Mo/TOC, V,

V/TOC trends is provided in Table S2 and new data for this study are included in Table S3. The current compilation (Fig. 3) provides evidence for a significant ocean–atmosphere oxygenation event closely associated with the glacial retreat of the Marinoan ‘Snowball Earth’ event.

References

1. Condon, D. et al. U-Pb ages from the Neoproterozoic Doushantuo Formation, China. *Science* **308**, 95–98 (2005).
2. Zhang, S., Jiang, G., & Han, Y. The age of the Nantuo Formation and Nantuo glaciation in South China. *Terra Nova* **20**, 289–294 (2008).
3. McFadden, K.A. et al. Pulsed oxidation and biological evolution in the Ediacaran Doushantuo Formation. *Proc. Natl. Acad. Sci. USA* **105**, 3197–3202 (2008).
4. Zhu, M. et al. Integrated Ediacaran (Sinian) chronostratigraphy of South China: *Palaeogeogr. Palaeoclimatol. Palaeoecol.* **254**, 7–61 (2007).
5. Zhou, C. et al. The diversification and extinction of Doushantuo–Pertatataka acritarchs in South China: causes and biostratigraphic significance: *Geol. J.* **42**, 229–262 (2007).
6. Jiang, G. et al. Stratigraphy and paleogeography of the Ediacaran Doushantuo Formation (ca. 635–551 Ma) in South China. *Gondwana Res.* **19**, 831–849 (2011).
7. Jiang, G. et al. Stable isotopic evidence for methane seeps in Neoproterozoic postglacial cap carbonates: *Nature* **426**, 822–826 (2003).
8. Jiang, G. et al. Stratigraphy, Sedimentary Structures, and Textures of the Late Neoproterozoic Doushantuo Cap Carbonate in South China: *J. Sediment. Res.* **76**, 978–995 (2006).
9. Wang, J., & Li, Z.-X. History of Neoproterozoic rift basins in South China: implications for Rodinia break-up: *Precambrian Res.* **122**, 141–158 (2003).

10. Jiang, G., Sohl, L.E., & Christie-Blick, N. Neoproterozoic stratigraphic comparison of the Lesser Himalaya (India) and Yangtze Block (South China); paleogeographic implications: *Geology*, **31**, 917-920 (2003).
11. Liu, B. et al. Paleocontinental sediments, crust evolution and ore deposits of South China. *Science Press, Beijing*, 236 (1993).
12. Li, C. et al. A stratified redox model for the Ediacaran ocean. *Science* **328**, 80-83 (2010).
13. Bristow, T.F. et al. Mineralogical constraints on the paleoenvironments of the Ediacaran Doushantuo Formation: *Proc. Natl. Acad. Sci. USA* **106**, 13190-13195 (2009).
14. Hoffman, P.F. et al. Are basal Ediacaran (635 Ma) post-glacial "cap dolostones" diachronous?: *Earth Planet. Sci. Lett.* **258**, 114-131 (2007).
15. Rose, C.V., and Maloof, A.C. Testing models for post-glacial 'cap dolostone' deposition: Nuccaleena Formation, South Australia: *Earth Planet. Sci. Lett.* **296**, 165-180 (2010).
16. Jiang, G. et al. Organic carbon isotope constraints on the dissolved organic carbon (DOC) reservoir at the Cryogenian-Ediacaran transition: *Earth Planet. Sci. Lett.* **299**, 159-168 (2010).
17. Zhou, C. et al. Timing the deposition of ^{17}O -depleted barite at the aftermath of Nantuo glacial meltdown in South China: *Geology*, **38**, 903-906 (2010).
18. Vernhet, E. et al. Stratigraphic reconstruction of the Ediacaran Yangtze platform margin (Hunan province, China) using a large olistolith: *Palaeogeogr. Palaeoclimatol. Palaeoecol.* **254**, 123-139 (2007).
19. Liu, P. et al. New material of microfossils from the Ediacaran Doushantuo Formation in the Zhangcunping area, Yichang, Hubei Province and its zircon SHRIMP U-Pb age: *Chinese Sci. Bul.* **54**, 1058-1064 (2009).

20. Xiao, S., Zhang, Y., & Knoll, A.H. Three-dimensional preservation of algae and animal embryos in a Neoproterozoic phosphorite. *Nature* **391**, 553-558 (1998).
21. Yin, L. et al. Doushantuo embryos preserved inside diapause egg cysts. *Nature* **446**, 661-663 (2007).
22. Yuan et al. An early Ediacaran assemblage of macroscopic and morphologically differentiated eukaryotes. *Nature* **470**, 390-393 (2011).
23. Erwin, D.H. et al. The Cambrian conundrum: Early divergence and later ecological success in the early history of animals. *Science* **334**, 1091-1097 (2011).
24. Love, G.D. et al. Fossil steroids record the appearance of Demospongiae during the Cryogenian period. *Nature* **457**, 718-721 (2009).
25. Maloof, A.C. et al. Possible animal-body fossils in pre-Marinoan limestones from South Australia. *Nature Geosci.* **3**, 653-659 (2010).
26. Brain, C.K.B. et al. The first animals: ca. 760 million-year-old sponge-like fossils from Namibia. *S. Afr. J. Sci.* **108**, 658 (2012).
27. Neuweiler, F., Turner, E.C., Burdige, D.J. Early Neoproterozoic origin of the metazoan clade recorded in carbonate rock texture. *Geology* **37**, 475–478 (2009).
28. Planavsky, N. Early Neoproterozoic origin of the metazoan clade recorded in carbonate rock texture: Comment. *Geology* **37**, e195 (2009).
29. Hoffmann, Friederike et al. Oxygen dynamics and transport in the Mediterranean sponge *Aplysina aerophoba*. *Marine Biology* **153**, 1257-1264 (2008).
30. Hultgren, T. et al. Fossilized nuclei and germination structures identify Ediacaran “animal embryos” as encysting protists. *Science* **334**, 1696-1699 (2011).

31. Xiao, S. et al. Comment on “Fossilized nuclei and germination structures identify Ediacaran ‘animal embryos’ as encysting protists”. *Science* **335**, 1169c.(2012).
32. Schiffbauer, J.D. et al. The origin of intracellular structures in Ediacaran metazoan embryos. *Geology* **40**, 223-226 (2012).
33. Peterson, K.J., & Butterfield, N.J. Origin of the Eumetazoa: Testing ecological predictions of molecular clocks against the Proterozoic fossil record: *Proc. Natl. Acad. Sci. USA* **102**, 9547-9552 (2005).
34. Butterfield, N. J, Oxygen, animals and oceanic ventilation: an alternative view. *Geobiology* **7**, 1-7 (2009).
35. Smetacek, V. A watery arms race. *Nature* **411**, 745 (2001).
36. Pecoits, E. et al. Bilaterian Burrows and Grazing Behavior at >585 Million Years Ago. *Science* **336**, 1693-1696 (2012).
37. Liu, A. G., McLlroy, D., & Brasier, M. D. First evidence for locomotion in the Ediacara biota from the 565 Ma Mistaken Point Formation, Newfoundland. *Geology* **38**, 123–126 (2010).
38. Ivantsov, A.Y. New reconstruction of *Kimberella*, problematic Vendian metazoan. *Paleontol. J.* **43**, 601–611 (2009).
39. Kendall, B. et al. Pervasive oxygenation along late Archaean ocean margins. *Nature Geosci.* **3**, 647-652 (2010).
40. Poulton, S.W., Fralick, P.W. & Canfield, D.E. The transition to a sulphidic ocean ~1.84 billion years ago. *Nature* **431**,173-177 (2004).
41. Scott, C. et al. Tracing the stepwise oxygenation of the Proterozoic ocean. *Nature* **452**, 456-459 (2008).

42. Poulton, S. W. & Canfield, D. E. Development of a sequential extraction procedure for iron: implications for iron partitioning in continentally derived particulates. *Chem. Geol.* **214**, 209–221 (2005).
43. Och, L.M., & Shields-Zhou, G.A. The Neoproterozoic oxygenation event: Environmental perturbations and biogeochemical cycling. *Earth-Sci. Rev.* **110**, 26-57 (2012).
44. Tribovillard, N. et al. Trace metals as paleoredox and paleoproductivity proxies: an update. *Chem. Geol.* **232**, 12-32 (2006).
45. Algeo, T. J. & Lyons, T. W. Mo-total organic carbon covariation in modern anoxic marine environments: Implications for analysis of paleoredox and paleohydrographic conditions. *Paleoceanography* **21**, PA001112 (2006).
46. Lyons, T. W. et al. Tracking euxinia in the ancient ocean: A multiproxy perspective and Proterozoic case study. *Annu. Rev. Earth Pl. Sci.* **37**, 507-534 (2009).
47. Emerson, S. R. & Huested, S. S. Ocean anoxia and the concentrations of molybdenum and vanadium in seawater. *Mar. Chem.* **34**, 177-196 (1991).
48. Hastings D.W., Emerson, S.R. & Mix, A.C. Vanadium in foraminiferal calcite as a tracer for changes in the areal extent of reducing sediments. *Paleoceanography* **11**, 665-678 (1996).
49. Morford, J. L. et al. Diagenesis of oxyanions (V, U, Re, and Mo) in pore waters and sediments from a continental margin. *Geochim. Cosmochim. Acta* **69**, 5021-5032 (2005).
50. Miller, C.A. et al. Re-assessing the surface cycling of molybdenum and rhenium. *Geochim. Cosmochim. Acta* **75**, 7146-7179 (2011).
51. McManus, J. et al. Molybdenum and uranium geochemistry in continental margin sediments: Paleoproxy potential. *Geochim. Cosmochim. Acta* **70**, 4643-4662 (2006).

52. Brucker, R. L. P. et al. Molybdenum behavior during early diagenesis: Insights from Mo isotopes. *Geochem. Geophys. Geosys.* **10**, (2009).
53. Raiswell, R. & Canfield, D.E. Sources of iron for pyrite formation in marine sediments. *Am. J. Sci.* **298**, 219-245 (1998).
54. Lyons, T.W. & Severmann, S. A critical look at iron paleoredox proxies based on new insights from modern euxinic marine basins. *Geochim. Cosmochim. Acta* **70**, 5698-5722 (2006).
55. Severmann, S. et al. Modern iron isotope perspective on the benthic iron shuttle and the redox evolution of ancient oceans. *Geology* **36**, 487-490 (2008).
56. Wedepohl, K. H. The composition of the continental crust. *Geochim. Cosmochim. Acta* **59**, 1217-1232 (1995).
57. Li, Z.X. et al. Assembly, configuration, and break-up history of Rodinia: A synthesis. *Precambrian Res.* **160**, 179-210 (2008).
58. Hoffman, P.F., & Li, Z.-X. A palaeogeographic context for Neoproterozoic glaciation. *Palaeogeogr. Palaeoclimatol. Palaeoecol.* **277**, 158-172 (2009).
59. Anbar, A. D. & Knoll, A. H. Proterozoic ocean chemistry and evolution: A bioinorganic bridge? *Science* **297**, 1137–1142 (2002).
60. Helz, G. R., Bura-Nakić, E., Mikac, N. & Ciglencčki, I. New model for molybdenum behavior in euxinic waters. *Chem. Geol.* **284**, 323-332 (2011).
61. Poulson, R.L., Siebert, C., McManus, J., & Berelson, W.M. Authigenic molybdenum isotope signatures in marine sediments. *Geology* **34**, 617-620 (2006).
62. Xiao, S. et al. Integrated chemostratigraphy of the Doushantuo Formation at the northern Xiaofenghe section (Yangtze Gorges, South China) and its implication for Ediacaran

- stratigraphic correlation and ocean redox models. *Precambrian Res.* **192-195**, 125-141 (2012).
63. Shields, G. et al. Sulphur isotopic evolution of Neoproterozoic-Cambrian seawater: new francolite-bound sulphate $\delta^{34}\text{S}$ data and a critical appraisal of the existing record. *Chem. Geol.* **204**, 163-182 (2004).
64. Sim, M.S., Bosak, T., & Ono, S. Large sulfur isotope fractionation does not require disproportionation. *Science* **333**, 74-77 (2011).
65. Canfield, D.E., Farquhar, J., & Zerkle, A.L. High isotope fractionations during sulfate reduction in a low-sulfate euxinic ocean analog. *Geology* **38**, 415-418 (2010).
66. Canfield, D.E. & Raiswell, R. The evolution of the sulfur cycle. *Am. J. Sci.* **299**, 697-723 (1999).
67. Canfield, D.E. & Farquhar, J. Animal evolution, bioturbation, and the sulfate concentration of the oceans. *Proc. Natl. Acad. Sci. USA* **106**, 8123-8127 (2009).
68. Halverson, G.P. & Hurtgen, M.T. Ediacaran growth of the marine sulfate reservoir. *Earth Planet. Sci. Lett.* **263**, 32-44 (2007).
69. Kendall, B., Creaser, R.A., Calver, C.R., Raub, T.D., & Evans, D.A.D. Correlation of Sturtian diamictite successions in southern Australia and northwestern Tasmania by Re-Os black shale geochronology and the ambiguity of “Sturtian”-type diamictite-cap carbonate pairs as chronostratigraphic marker horizons. *Precambrian Res.* **172**, 301-310 (2009).
70. Li, C. et al. Evidence for a redox stratified Cryogenian marine basin, Datangpo Formation, South China. *Earth Planet. Sci. Lett.* **331-332**, 246-256 (2012).

71. Jiang, S.Y. et al. Extreme enrichment of polymetallic Ni-Mo-PGE-Au in lower Cambrian black shales of South China: An Os isotope and PGE geochemical investigation. *Palaeogeogr. Palaeoclimatol. Palaeoecol.* **254**, 217–228 (2007).

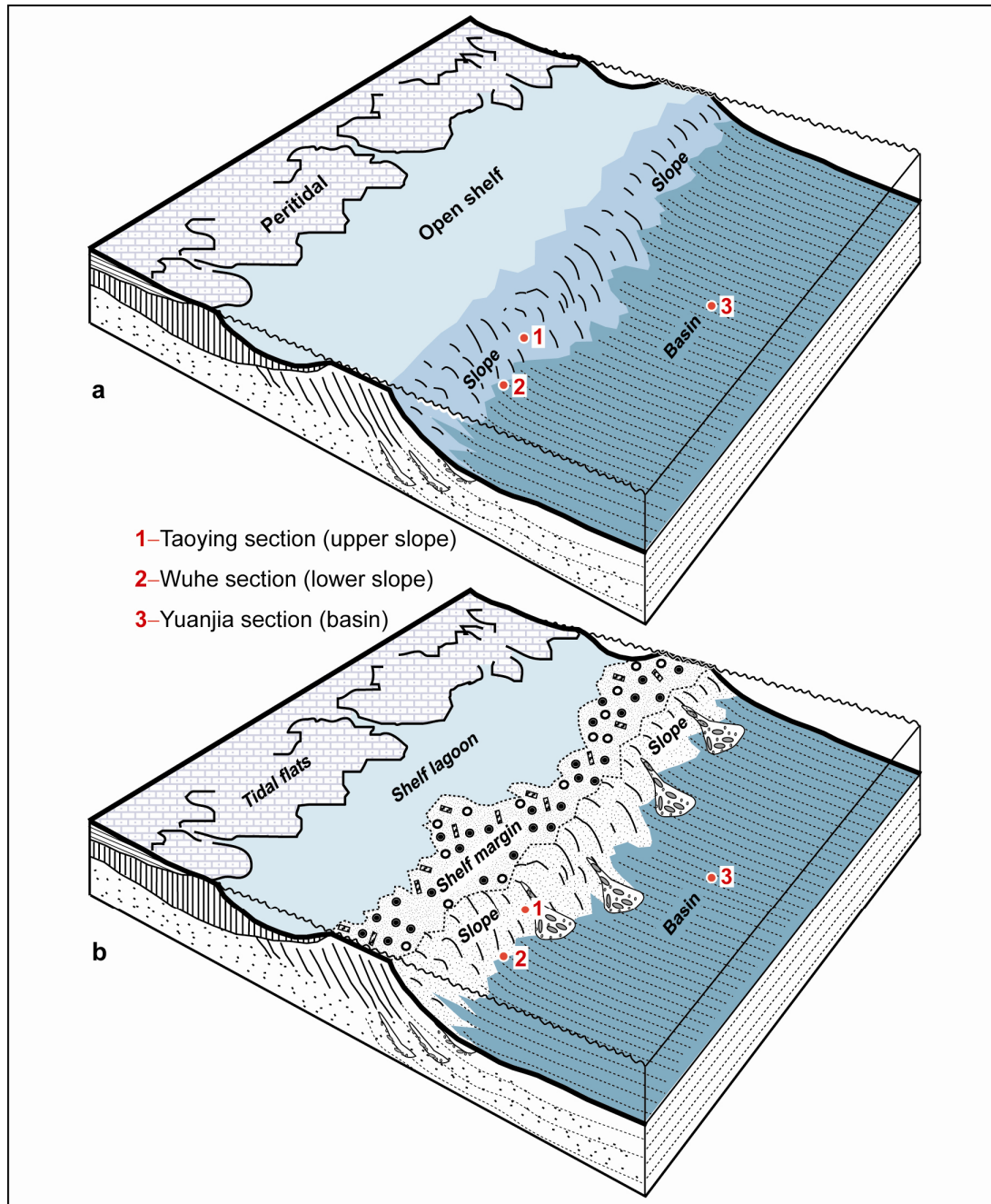


Figure S1 Paleogeographic reconstruction of the Ediacaran Yangtze platform during the deposition of the Doushantuo Formation (ca. 635–551 Myr)⁶. **a**, open shelf for the lower Doushantuo Formation. **b**, rimmed shelf for the middle and upper Doushantuo Formation. The depositional setting for the sampled interval (lower Doushantuo Formation) is illustrated in (a). Sampled sections are from the slope (loc. 1 & 2) and basin (loc. 3) settings that were below the storm wave base and were well connected with the open ocean. Paleobathymetric estimation is based on the continental slope gradient¹¹ and accommodation space of Cambrian–early Silurian stratigraphic units (backstripping analysis)^{8,10}. The water depth of the basinal section (loc. 3) is estimated to have been greater than 1000 m.

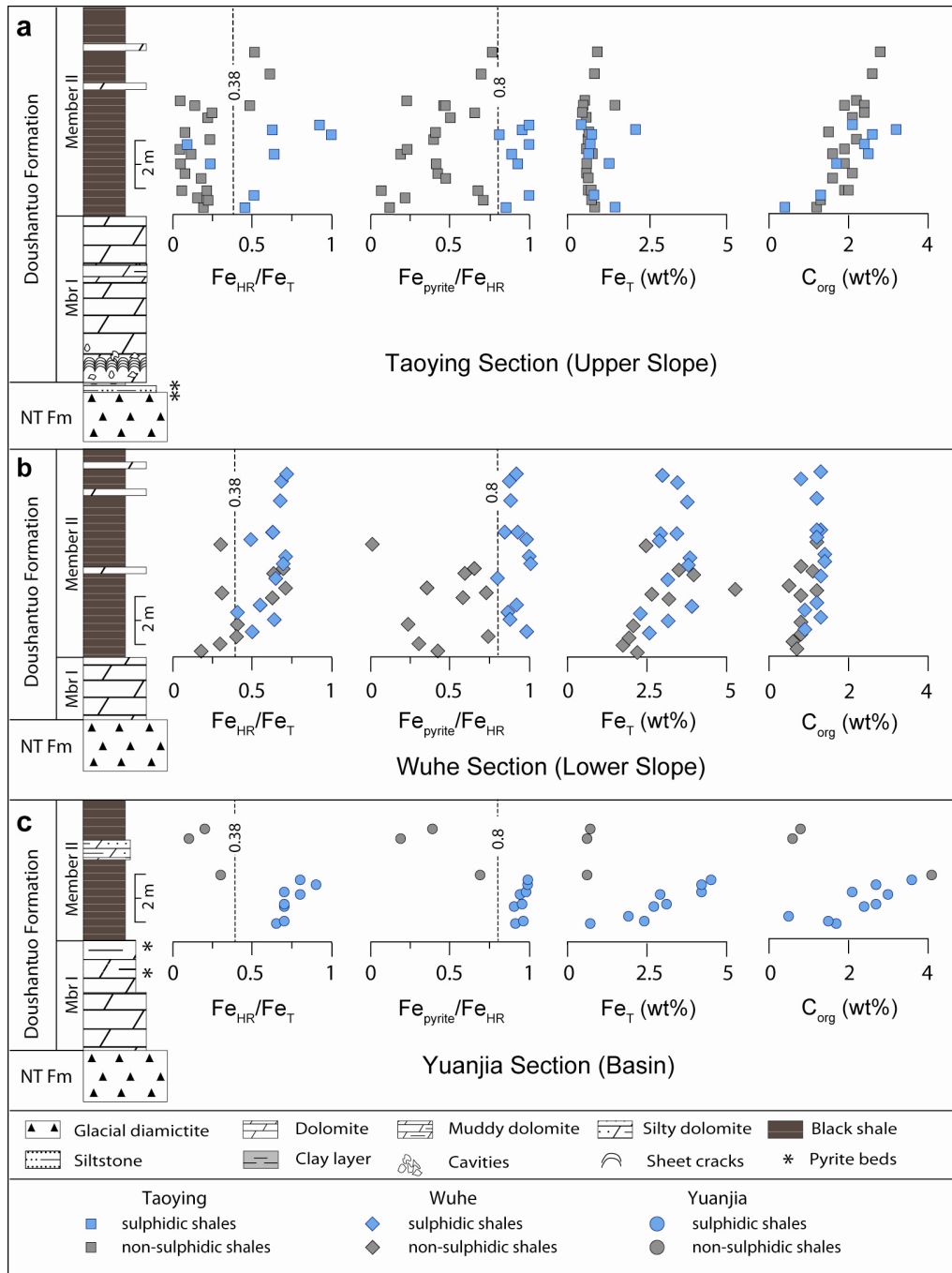


Figure S2 Iron speciation data of the lower Doushantuo Formation. **a**, Taoying section (upper slope). **b**, Wuhe section (lower slope). **c**, Yuanjia section (basin). Submeter-scale variations in Fe_{HR}/Fe_T and Fe_{pyrite}/Fe_T likely record dynamic redox fluctuations characterized by alternating oxic, suboxic, and anoxic local environments. However, when Fe_T values and Fe_T/Al ratios are significantly lower than average crustal values, using Fe_{HR}/Fe_T to distinguish anoxic vs. oxic environments needs to be done with caution. When Fe_T values are low, high Fe_{HR}/Fe_T (> 0.38) with low Fe_{pyrite}/Fe_{HR} (< 0.8) values indicative of ferruginous conditions may in fact record oxic conditions, while high Fe_{HR}/Fe_T (> 0.38) with high Fe_{pyrite}/Fe_{HR} (> 0.8) values could potentially record sulphidic conditions in porewaters.

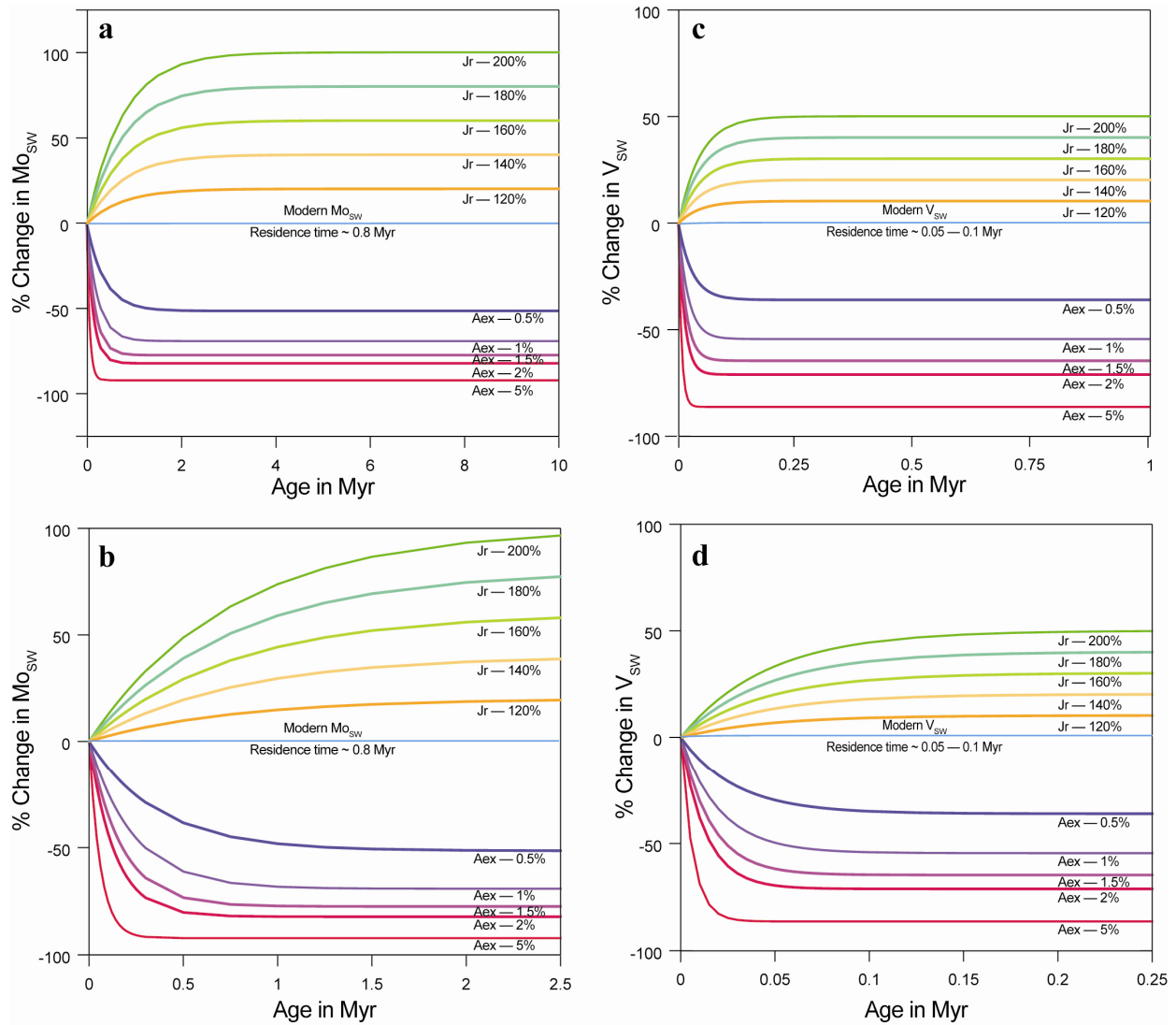


Figure S3 Model results for seawater Mo and V changes through time. **a, b**, Changes in seawater Mo concentrations in response to increase of riverine flux of Mo (Jr) through enhanced weathering and to increase of anoxic/euxinic environments (Aex) in the ocean. **c, d**, Changes in seawater V concentrations in response to increase of riverine flux of V (Jr) and to increase of anoxic/euxinic environments (Aex). Note that **b** and **d** are the same modeling results of **a** and **c**, respectively, with enlarged time scales. A small percentage increase in anoxic seafloor of the continental margin can crash the ocean Mo and V reservoirs within a much shorter period than doubling the riverine flux. Therefore, we interpret that Phanerozoic-like Mo and V enrichments in the lower Doushantuo black shales record a major oxygenation event following the Marinoan glacial retreat.

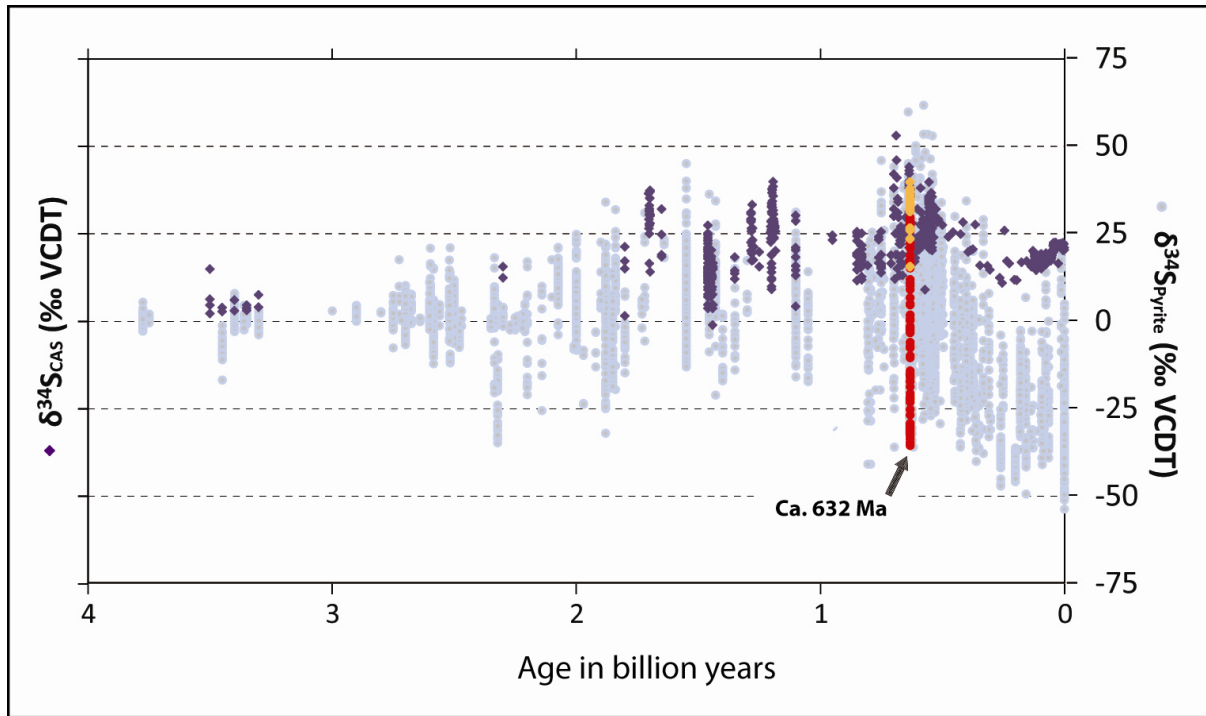


Figure S4 Sulphur isotope composition of sedimentary sulphide ($\delta^{34}\text{S}_{\text{pyrite}}$) and carbonate associated sulphate ($\delta^{34}\text{S}_{\text{CAS}}$) through time. The compilation is modified from Canfield & Farquhar (2009)⁶⁷ and Och & Shields (2012)⁴³, with the lower Doushantuo Formation $\delta^{34}\text{S}_{\text{CAS}}$ (yellow diamonds) and $\delta^{34}\text{S}_{\text{pyrite}}$ (red circles) data added and marked.

Supplementary Table S1 Iron speciation, TOC, and trace elemental data from the lower Doushantuo Formation (Memebr II) shales

Taoying section, Guizou Province, South China (Upper Slope)

Section 1a. 7.3 m is the end of Cap Carbonate

Sample No.	C _{org} (Wt %)	TIC (Wt %)	δ ³⁴ S _{pyrite}	Fe _{Mag} (Wt %)	Fe _{Oxide} (Wt %)	Fe _{Carb} (Wt %)	Fe _{pyrite} (Wt %)	Fe _{HR}	Fe _T (Wt %)	Fe _{pyrite} /Fe _{HR}	Fe _{HR} /Fe _T	Al (Wt %)	Mo (ppm)	Mo/TOC ppm/wt%	V ppm	V/TOC ppm/wt%	U (ppm)	U/TOC ppm/wt%
TY09-7.6	1.2	0.0	n.d	0.0	0.1	0.0	0.0	0.2	0.8	0.1	0.3	7.4	3.2	2.7	5900	4962	17.9	15.0
TY09-7.9	1.3	0.0	n.d	0.0	0.1	0.0	0.2	0.2	0.7	0.7	0.3	7.7	3.7	3.0	3973	3178	11.3	9.0
TY09-8	1.3	0.0	n.d	0.0	0.1	0.0	0.0	0.2	0.7	0.2	0.2	8.1	1.3	1.0	3950	3080	16.7	13.1
TY09-8.3	1.9	0.0	-3.3	0.0	0.1	0.0	0.0	0.1	0.6	0.1	0.1	8.4	2.8	1.5	2946	1545	16.9	8.9
TY09-8.6	1.5	0.0	4.60	0.0	0.0	0.0	0.0	0.1	0.7	0.2	0.1	7.9	24.8	16.7	285	193	3.8	2.5
TY09-8.8	1.6	0.0	n.d	0.0	0.1	0.0	0.1	0.2	0.6	0.5	0.3	8.7	6.4	4.0	1767	1095	18.4	11.4
TY09-9	2.1	0.0	n.d	0.0	0.0	0.0	0.0	0.1	0.6	0.4	0.2	8.2	4.1	1.9	1451	689	19.1	9.1
TY09-9.4	1.9	0.0	n.d	0.0	0.0	0.0	0.0	0.1	0.6	0.4	0.1	8.6	5.4	2.8	950	489	18.0	9.2
TY09-9.8	1.6	0.0	n.d	0.0	0.1	0.0	0.0	0.1	0.8	0.2	0.2	9.5	2.9	1.8	1516	971	23.7	15.2
TY09-10	1.9	0.0	-5.96	0.0	0.0	0.0	0.0	0.1	0.6	0.2	0.1	8.3	3.1	1.6	835	440	18.7	9.9
TY09-10.2	2.4	0.0	-15.7	0.0	0.0	0.0	0.1	0.1	0.7	1.0	0.2	9.8	29.3	12.3	1178	493	18.5	7.7
TY09-10.4	2.2	0.0	n.d	0.0	0.1	0.0	0.1	0.2	0.6	0.4	0.3	7.7	39.5	18.1	804	369	17.2	7.9
TY09-10.7	1.5	0.0	n.d	0.0	0.0	0.0	0.0	0.1	0.7	0.4	0.2	8.9	11.3	7.3	1853	1196	19.4	12.5
TY09-11	2.1	0.0	-9.9	0.0	0.0	0.0	0.5	0.5	0.4	1.0	1.0	5.5	30.0	14.2	525	249	10.3	4.9
TY09-11.3	2.1	0.0	n.d	0.0	0.1	0.0	0.1	0.2	0.6	0.5	0.3	7.3	11.3	5.3	253	118	8.2	3.8
TY09-11.5	2.4	0.0	n.d	0.0	0.0	0.0	0.1	0.1	0.5	0.7	0.3	7.1	10.6	4.5	247	105	8.0	3.4
TY09-11.8	2.4	0.0	n.d	0.0	0.0	0.0	0.0	0.1	0.5	0.5	0.2	7.2	10.8	4.5	213	88	8.4	3.5
TY09-12	2.2	0.0	n.d	0.0	0.0	0.0	0.0	0.1	0.5	0.2	0.1	7.6	6.2	2.8	294	131	7.7	3.5

Section 1b. 13.0 m is the base of the black shale

TY09-13.3	0.4	0.0	n.d	0.0	0.1	0.0	0.7	0.8	1.5	0.9	0.5	8.3	1.4	4.0	1016	2783	7.8	21.4
TY09-13.8	1.3	0.0	-7.6	0.0	0.0	0.0	0.5	0.5	0.8	1.0	0.6	9.0	3.5	2.6	6096	4582	13.1	9.8
TY09-14	2.0	0.0	n.d	0.0	0.1	0.0	0.1	0.2	0.7	0.7	0.3	8.8	14.5	7.2	3040	1499	19.1	9.4
TY09-15.1	1.7	0.0	-26.8	0.0	0.0	0.0	0.4	0.4	1.3	0.9	0.3	19.4	38.2	22.2	2522	1465	33.6	19.5
TY09-15.5	2.5	0.0	n.d	0.0	0.0	0.0	0.4	0.5	0.6	0.9	0.7	7.7	165.3	67.0	669	271	15.7	6.4
TY09-16.3	2.6	0.0	n.d	0.0	0.1	0.0	0.7	0.8	0.7	0.8	1.1	8.8	48.4	18.7	455	176	16.8	6.5
TY09-16.5	3.2	0.0	-31.6	0.0	0.1	0.0	1.4	1.5	2.1	1.0	0.7	8.9	114.4	35.6	424	132	12.5	3.9
TY09-17.5	1.9	0.0	-23.1	0.0	0.4	0.0	0.4	0.8	1.5	0.5	0.6	8.8	13.0	7.0	418	224	5.7	3.0
TY09-18.8	2.6	0.0	-22.3	0.0	0.2	0.0	0.4	0.6	0.8	0.7	0.7	6.7	9.0	3.5	262	101	3.8	1.5
TY09-19.7	2.8	0.0	-22.1	0.0	0.1	0.0	0.4	0.5	0.9	0.8	0.6	7.2	11.5	4.2	313	114	4.7	1.7
TY09-21.3	4.5	0.0	-16.0	0.0	0.1	0.0	0.9	1.0	0.6	0.9	1.0	6.1	12.1	2.7	200	44	6.8	1.5
TY09-22.3	1.0	0.0	0.2	0.0	0.0	0.0	1.5	1.5	1.0	1.0	1.0	5.5	0.3	0.3	185	181	5.4	5.2

Wuhe section, Guizou Province, South China (Lower Slope)

Section 2. 2.3 m is the end of Cap Carbonate

Sample No.	C _{org} (Wt %)	TIC (Wt %)	δ ³⁴ S _{pyrite}	Fe _{Mag} (Wt %)	Fe _{Oxide} (Wt %)	Fe _{Carb} (Wt %)	Fe _{pyrite} (Wt %)	Fe _{HR}	Fe _T (Wt %)	Fe _{pyrite} /Fe _{HR}	Fe _{HR} /Fe _T	Al (Wt %)	Mo (ppm)	Mo/TOC ppm/wt%	V ppm	V/TOC ppm/wt%	U (ppm)	U/TOC ppm/wt%
WH09-2.4	0.7	0.0	n.d	0.0	0.2	0.0	0.2	0.4	2.2	0.4	0.2	10.4	0.6	0.8	4438	6124	13.4	18.4
WH09-2.7	0.6	0.0	-17.2	0.1	0.3	0.0	0.1	0.5	1.7	0.3	0.3	8.7	8.7	14.2	1824	2994	12.3	20.2
WH09-3	0.8	0.2	-32.3	0.0	0.1	0.1	0.6	0.8	1.9	0.7	0.4	8.4	3.8	4.6	584	707	14.0	16.9
WH09-3.2	0.9	0.0	-32.8	0.0	0.0	0.0	1.2	1.3	2.6	1.0	0.5	8.6	38.0	40.5	489	522	13.8	14.7
WH09-3.5	0.8	0.0	-34.6	0.2	0.4	0.0	0.2	0.8	2.1	0.2	0.4	9.4	2.5	3.0	390	485	13.8	17.2
WH09-3.7	1.3	0.0	-33.7	0.1	0.1	0.1	1.7	2.0	3.2	0.9	0.6	9.0	62.3	49.7	333	266	15.8	12.6
WH09-4	0.9	0.1	-32.8	0.0	0.1	0.0	0.7	0.9	2.3	0.9	0.4	8.7	7.8	8.6	324	356	14.0	15.4
WH09-4.3	1.2	0.0	-34.9	0.0	0.0	0.1	1.9	2.1	3.9	0.9	0.5	9.4	172.3	144.9	288	242	12.6	10.6
WH09-4.6	0.8	2.1	-29.1	0.0	0.1	0.7	1.1	2.0	3.2	0.6	0.6	6.6	11.2	14.6	208	272	9.8	12.8
WH09-4.8	1.2	0.2	-30.6	0.0	0.1	0.1	0.6	0.8	2.6	0.7	0.3	8.5	13.5	11.6	241	208	10.0	8.6
WH09-5	0.5	7.5	-26.8	0.4	0.0	2.0	1.3	3.7	5.3	0.3	0.7	3.4	39.5	84.7	171	367	5.5	11.9
WH09-5.4	1.3	1.4	-32.4	0.0	0.0	0.4	1.6	2.0	3.14	0.8	0.6	8.47	41.21	32.0	185	144	5.84	4.5
WH09-5.6	1.1	3.5	-30.5	0.0	0.1	0.9	1.4	2.5	3.96	0.6	0.6	7.03	42.42	37.9	199	178	5.34	4.8
WH09-5.8	0.8	3.1	-29.8	0.0	0.1	0.8	1.5	2.4	3.49	0.6	0.7	6.64	21.92	27.7	213	270	3.87	4.9
WH09-6.0	1.4	0.0	-33.7	0.0	0.0	0.0	2.6	2.6	3.79	1.0	0.7	9.99	29.94	22.0	212	156	4.36	3.2
WH09-6.3	1.4	0.0	-33.5	0.0	0.0	0.0	2.7	2.7	3.84	1.0	0.7	10.13	27.25	19.6	213	153	3.87	2.8
WH09-6.5	1.2	0.0	-32.5	0.0	0.7	0.0	0.0	0.7	2.46	0.0	0.3	9.33	58.11	50.4	184	160	4.25	3.7
WH09-6.8	1.2	0.0	-32.4	0.0	0.0	0.0	1.3	1.4	2.88	1.0	0.5	9.63	37.62	31.5	207	173	5.22	4.4
WH09-7.0	1.2	0.1	-31.1	0.0	0.0	0.1	1.9	2.1	3.43	0.9	0.6	9.15	26.05	22.6	221	192	3.68	3.2
WH09-7.3	1.3	0.5	-30.0	0.0	0.0	0.3	1.5	1.8	2.9	0.8	0.6	8.2	12.6	9.9	174	136	5.1	4.0
WH09-8.6	1.2	0.8	-31.6	0.0	0.0	0.3	2.2	2.5	3.76	0.9	0.7	8.65	23.95	20.5	170	145	2.94	2.5
WH09-9.4	0.8	0.5	-31.7	0.0	0.1	0.2	2.0	2.3	3.4	0.9	0.7	7.8	8.0	10.1	170	216	5.9	7.5
WH09-9.7	1.3	0.2	-32.0	0.0	0.0	0.2	1.9	2.1	3.0	0.9	0.7	7.9	11.5	9.1	134	106	4.2	3.3
WH09-11.6	1.3	0.0	-30.1	0.0	0.0	0.1	1.9	2.0	3.0	1.0	0.7	6.8	11.9	9.5	143	114	3.6	2.8
WH09-13.7	0.6	4.0	-21.0	0.0	0.0	0.7	1.6	2.2	2.5	0.7	0.9	4.2	3.9	6.5	94	156	3.9	6.5

Yuanjia Section, Hunan Province, South China (Basinal)

Section 3. 4.6 m is the end of Cap Carbonate

Sample No.	C _{org} (Wt %)	TIC (Wt %)	δ ³⁴ S _{pyrite}	Fe _{Mag} (Wt %)	Fe _{Oxide} (Wt %)	Fe _{Carb} (Wt %)	Fe _{pyrite} (Wt %)	Fe _{HR}	Fe _T (Wt %)	Fe _{pyrite} /Fe _{HR}	Fe _{HR} /Fe _T	Al (Wt %)	Mo (ppm)	Mo/TOC ppm/wt%	V ppm	V/TOC ppm/wt%	U (ppm)	U/TOC ppm/wt%
WHH-5.6	1.7	0.0	-14.2	0.0	0.0	0.0	0.4	0.4	0.7	0.9	0.65	9.9	13.4	7.7	6417	3680	9.3	5.3
WHH-5.7	1.5	0.0	-26.7	0.0	0.1	0.0	1.6	1.7	2.4	0.9	0.7	9.6	64.3	43.8	2767	1884	17.9	12.2
WHH-5.9	1.6	-	-	-	-	-	-	-	1.9	-	-	9.4	120.1	75.1	-	-	-	-
WHH-6.3	2.4	0.0	-30.3	0.0	0.1	0.2	1.7	1.9	2.7	0.9	0.7	8.8	135.9	55.6	1193	488	19.7	8.1
WHH-6.4	2.7	0.0	-31.7	0.0	0.1	0.1	2.1	2.3	3.1	0.9	0.7	8.7	148.0	55.3	847	317	20.1	7.5
WHH-6.8	3.0	0.0	-35.5	0.0	0.0	0.2	2.3	2.5	2.9	0.9	0.8	7.6	97.3	32.3	497	165	12.5	4.1
WHH-6.9	2.1	0.0	-25.2	0.0	0.0	0.1	2.8	2.9	4.2	1.0	0.7	8.6	25.2	12.1	370	178	11.0	5.3
WHH-7.2	2.7	0.0	n.d	0.0	0.0	0.1	3.5	3.7	4.2	1.0	0.9	7.1	37.3	13.8	-	-	8.8	3.3
WHH-7.4	3.6	0.0	-30.2	0.0	0.0	0.1	3.5	3.7	4.5	1.0	0.8	7.4	36.7	10.1	336	93	10.1	2.8
WHH-7.6	4.1	0.0	-21.4	0.0	0.1	0.0	0.1	0.2	0.6	0.7	0.3	8.5	10.6	2.6	458	113	8.7	2.1
WHH-9.1	0.6	0.0	-7.0	0.0	0.0	0.0	0.0	0.1	0.6	0.2								

Supplementary Table S2 Reference list used for the compilation of the secular trends of Mo, Mo/TOC, V, and V/TOC (Figure 3)

Age (Ga)	Formation	Location	Reference/Source
0.000	Black Sea Unit 2		Brumsack, H. J., <i>Palaeogeogr. Palaeoclimatol. Palaeoecol.</i> 232 , 344-361 (2006).
0.000	Sapropel sediments	Tyrrhenian Basin, western Mediterranean	Gehrke et al., <i>Geochim. Cosmochim. Acta</i> 73 , 1651-1665 (2009).
0.000	Peru Margin sediments	East Pacific	Böning, P. et al., <i>Geochim. Cosmochim. Acta</i> 68 , 4429-4451 (2004).
0.000	East Pacific Margin sediments	San Clemente, Chile Margin	McManus, J. et al., <i>Geochim. Cosmochim. Acta</i> 70 , 4643-4662 (2006).
0.000	East Pacific Margin sediments	Washington State, North Pacific	Morford, J. L. et al., <i>Geochim. Cosmochim. Acta</i> 69 , 5021-5032 (2005).
0.000	Microlaminated sediments	Cariaco Basin, Venezuela	Lyons, T.W. et al., <i>Chem. Geol.</i> 195 (1-4), 131-157 (2003).
0.000	Anoxic sediments	Framvaren Fjord and Saanich Inlet	Algeo, T. J. & Lyons, T. W., <i>Paleoceanography</i> 21 , PA1016 (2006).
0.081	Julia Creek Oil Shale, Toolebuc Formation	Queensland, Australia	Hirner & Xu., <i>Chem. Geol.</i> 91 , 115-124 (1991).
0.086	La Luna Formation	Venezuela	Alberdi-Genolet & Tocco, <i>Chem. Geol.</i> 160 , 19-38 (1999).
0.091	C/T Demerara Rise	Demerara Rise	Brumsack, H. J., <i>Palaeogeogr. Palaeoclimatol. Palaeoecol.</i> 232 , 344-361 (2006).
0.113	Machiques Member	Venezuela	Alberdi-Genolet & Tocco, <i>Chem. Geol.</i> 160 , 19-38 (1999).
0.154	Kimmeridge Clay Formation	Yorkshire Coast, UK	Tribouillard, N.P. et al., <i>Palaeogeogr. Palaeoclimatol. Palaeoecol.</i> 108 , 165-181 (1994).
0.180	Whitby Mudstone Formation	Yorkshire Coast, UK	Pearce et al., <i>Geology</i> 36 , 231-234 (2008).
0.183	Lower Toarcian Shales	Yorkshire Coast, UK	McArthur, J.M., et al., <i>Paleoceanography</i> 23 , PA4217 (2008).
0.247	Kupferschiefer Shales	Northern Zechstein Basin, Poland	Pašava et al., <i>Miner. Deposita</i> 45 , 189-199 (2010).
0.305	Hushpuckney Shale Member, Coffeyville Fm	Oklahoma, USA	Cruse & Lyons, <i>Chem. Geol.</i> 206 , 319-345 (2004).
0.305	Stark Shale Member, Dennis Limestone	Wabaunsee County, Kansas	Hatch & Leventhal, <i>Chem. Geol.</i> 134 , 215-235 (1997).
0.309	Unnamed Shale Member	Osage Co, Oklahoma	Hatch & Leventhal, <i>Chem. Geol.</i> 134 , 215-235 (1997).
0.361	Sunbury Shale	Kentucky, USA	Perkins et al., <i>Palaeogeogr. Palaeoclimatol. Palaeoecol.</i> 265 , 14-29 (2008).
0.365	Ohio Shale, Cleveland Subunit	Kentucky, USA	Perkins et al., <i>Palaeogeogr. Palaeoclimatol. Palaeoecol.</i> 265 , 14-29 (2008).
0.365	Ohio Shale, Cleveland Subunit	Kentucky, USA	Dahl, T., et al., <i>Proc. Natl. Acad. Sci. USA</i> 107 , 17911-17915 (2010).
0.378	Marcellus Subgroup	New York, USA	Sageman, et al., <i>Chem. Geol.</i> 195 , 229-273 (2003).
0.388	Appalachian Devonian Shale	Pennsylvania, USA	Leventhal, J. S., <i>Miner. Deposita</i> 26 , 104-112 (1991).
0.388	Oatka Creek Formation	Livingston County, New York, USA	Werne et al., <i>Am. J. Sci.</i> 302 , 110-143 (2002).
0.392	Oatka Creek formation	New Albany Shale, USA	Gordon, G., et al., <i>Geology</i> 37 , 535-538 (2009).
0.440	Rastrites Shale, Birkhill Shale	Scotland and Sweden	Dahl, T., et al., <i>Proc. Natl. Acad. Sci. USA</i> 107 , 17911-17915 (2010).
0.465	Almelud Shale, Albjära, Gislövhammar	Tremadoc, Sweden	Dahl, T., et al., <i>Proc. Natl. Acad. Sci. USA</i> 107 , 17911-17915 (2010).
0.485	Alum Shale, Albjära, Gislövhammar	Tremadoc, Sweden	Dahl, T., et al., <i>Proc. Natl. Acad. Sci. USA</i> 107 , 17911-17915 (2010).
0.500	Alum Shale, Andrarum	Sweeden	Dahl, T., et al., <i>Proc. Natl. Acad. Sci. USA</i> 107 , 17911-17915 (2010).
0.515	Alum Shale	Närke Area, Sweden	Leventhal, J. S., <i>Miner. Deposita</i> 26 , 104-112 (1991).
0.526	Niutitang Formation	South China	Jiang, S. et al., <i>Miner. Deposita</i> 41 , 453-467 (2006).
0.526	Sugaitebulake	Northern Tarim Basin, China	Yuet et al., <i>J. Asian Earth Sci.</i> 34 , 418-436 (2009).
0.533	Niutitang Formation, Ganziping	China	Dahl, T., et al., <i>Proc. Natl. Acad. Sci. USA</i> 107 , 17911-17915 (2010).
0.540	Ara Group	Oman	Dahl, T., et al., <i>Proc. Natl. Acad. Sci. USA</i> 107 , 17911-17915 (2010).
0.542	Jiumenchong Fm.	Songtao section, South China	Guo, et al., <i>Palaeogeogr. Palaeoclimatol. Palaeoecol.</i> 254 , 194-216 (2007).
0.550	Upper Bhandar Shale	Vindhyan Basin, India	Paikaray et al., <i>J. Asian Earth Sci.</i> 32 , 34-48 (2008).
0.608	Old Fort Pt Fm.	Outcrop, Western Canada	Kendall et al., <i>Earth Planet. Sci. Lett.</i> 222 , 729-740 (2004).
0.620	Doushantuo Fm.	Songtao section, South China	Guo, et al., <i>Palaeogeogr. Palaeoclimatol. Palaeoecol.</i> 254 , 194-216 (2007).
0.625	Kuibis+Schwarzrand Subgroups, Nama Grp	Nama Group, Namibia	Laskowski & Kröner, <i>Geologische Rundschau</i> 74 , No.1, 1-9, (1985)
0.640	Black River Dolomite	Forest-1 Core, Australia and Tasmania	See Table S3
0.643	Tindelpina Shale Mbr	Blinman-2 and SCYW1a Core, Australia	Kendall et al., <i>Geology</i> 34 , 729-732 (2006).
0.650	Sirbu Shale	Vindhyan Basin, India	Paikaray et al., <i>J. Asian Earth Sci.</i> 32 , 34-48 (2008).
0.657	Aralka Fm	Wallara-1 Core, Australia	Kendall et al., <i>Geology</i> 34 , 729-732 (2006).
0.663	Datangpo Formation	South China	Li, C., et al., <i>Earth Planet. Sci. Lett.</i> 331-332 , 246-256 (2012)
0.700	Lower Bhandar Shale	Vindhyan Basin, India	Paikaray et al., <i>J. Asian Earth Sci.</i> 32 , 34-48 (2008).
0.715	Rewa Shale	Vindhyan Basin, India	Paikaray et al., <i>J. Asian Earth Sci.</i> 32 , 34-48 (2008).
0.750	AK-10-53-12	Chuar Group, Grand Canyon, USA	Dahl et al., <i>Earth Planet. Sci. Lett.</i> 311 , 264-274 (2011).
0.766	Rabanpalli Formation	India	Nagarajan et al., <i>Revista mexicana de ciencias geológicas</i> 24 , 150-160 (2007).
0.766	Mineral Fork Formation	Utah, USA	Young., G. M., <i>Geological Society of America Bulletin</i> 114 , p. 387-399 (2002).
0.771	Rabanpalli Formation	India	Nagarajan et al., <i>Revista mexicana de ciencias geológicas</i> 24 , 150-160 (2007).
0.800	Red Pine Shale	Uinta Mountains and Cottonwood Group	Condie et al., <i>Sediment. Geol.</i> 141-142 , 443-464 (2001).
0.940	Bijaygarh Shale	Vindhyan Basin, India	Paikaray et al., <i>J. Asian Earth Sci.</i> 32 , 34-48 (2008).
1.388	Olentangy Formation	Kentucky, USA	Perkins et al., <i>Palaeogeogr. Palaeoclimatol. Palaeoecol.</i> 265 , 14-29 (2008).
1.400	Velkerri Formation (Urapunga-4)	McArthur Basin, Northern Australia	Kendall et al., <i>Geochim. Cosmochim. Acta</i> 73 , 2534-2558 (2009).
1.400	Velkerri Formation, Roper Group	Roper Group, McArthur Basin	Arnold et al., <i>Science</i> 304 , 87-90 (2004).
1.600	Rampur Shale	Vindhyan Basin, India	Paikaray et al., <i>J. Asian Earth Sci.</i> 32 , 34-48 (2008).
1.630	Olive Shale	Vindhyan Basin, India	Paikaray et al., <i>J. Asian Earth Sci.</i> 32 , 34-48 (2008).
1.730	Wologorang Formation (Mount Young 2)	McArthur Basin, Northern Australia	Kendall et al., <i>Geochim. Cosmochim. Acta</i> 73 , 2534-2558 (2009).
1.800	RoveFormation	Canadian Sheild, Canada	Kendall et al., <i>Earth Planet. Sci. Lett.</i> 307 , 450-460 (2011).
1.800	RoveFormation	Canadian Sheild, Canada	Cameron & Garrels, <i>Chem. Geol.</i> 28 , 181-197 (1980).
1.800	Arangi Shale	Vindhyan Basin, India	Paikaray et al., <i>J. Asian Earth Sci.</i> 32 , 34-48 (2008).
1.900	DMH-23 (Black Shale)	Northeastern Labrador, Canada	Hayashi et al., <i>Geochim. Cosmochim. Acta</i> 61 , 4115-4137 (1997).
1.914	Morar Formation	Gwalior, India	Absar et al., <i>Precambrian Res.</i> 168 , 313-329 (2009).
2.000	Zaonezhskaya Formation	NW Russia	Melezhik et al., <i>Earth-Sci. Rev.</i> 47 , 1-40 (1999).
2.050	Zaonezhskaya Fm., Ludikovian Series	Karelia, Russia	See Table S3
2.150	Silverton Formation	Transvaal Supergroup, South Africa	Wronkiewicz et al., <i>Geochim. Cosmochim. Acta</i> 54 , 343-354 (1990).
2.350	Strubenkop Formation	Transvaal Supergroup, South Africa	Wronkiewicz et al., <i>Geochim. Cosmochim. Acta</i> 54 , 343-354 (1990).
2.400	Gowganda	Canadian Sheild, Canada	Cameron & Garrels, <i>Chem. Geol.</i> 28 , 181-197 (1980).
2.500	Jeerinah, Marra Mamba and Wittenoorn	Hammersley Basin, Australia	Alibert & McCulloch, <i>Geochim. Cosmochim. Acta</i> 57 , 187-204 (1993).
2.500	Gamohann/Kuruman	Transvaal Basin, South Africa	Beukes et al., <i>Economic Geology</i> 85 , 663-690 (1990).
2.500	Mt McRae Shale	ABDP-9 Core, Western Australia	Anbar et al., <i>Science</i> 317 , 1903-1906 (2007).
2.500	Klein Naute Formation-GKP01	South Africa	Kendall et al., <i>Nature Geosci.</i> 3 , 647-652 (2010).
2.530	Gamhaan Formation	South Africa	See Table S3
2.620	Jeerinah Formation, Fortescue Group	Australia	See Table S3
2.700	Sandur Superterrane	Bhimangundi, India	Manikyamba & Kerrich, <i>Geochim. Cosmochim. Acta</i> 70 , 4663-4679 (2006).
2.700	Bothaville Formation	Ventersdorp Supergroup, South Africa	Wronkiewicz et al., <i>Geochim. Cosmochim. Acta</i> 54 , 343-354 (1990).
2.700	Whim Creek Group	Western Australia	McLennan, et al., <i>Geochim. Cosmochim. Acta</i> 47 , 1211-1222 (1983).
2.700	Lac des Iles and Beardmore	Canadian Sheild, Canada	Cameron & Garrels, <i>Chem. Geol.</i> 28 , 181-197 (1980).
2.740	Michipicoten and Oba	Canadian Sheild, Canada	Cameron & Garrels, <i>Chem. Geol.</i> 28 , 181-197 (1980).
2.850	North Spirit Lake Greenstone Belt	Northwest Ontario, Canada	Nesbitt et al., <i>Precambrian Res.</i> 174 , 16-34 (2009).
2.900	Mozaan Group, Pongola Supergroup	Pongola Supergroup, S. Africa	Laskowski & Kröner, <i>Geologische Rundschau</i> 74 , No. 1, 1-9 (1985)
2.900	Red Lake	Canadian Sheild, Canada	Cameron & Garrels, <i>Chem. Geol.</i> 28 , 181-197 (1980).
3.000	Buhwa Greenstone Belt	Zimbabwe	Fedo et al., <i>Geochim. Cosmochim. Acta</i> 60 , 1751-1763 (1996).
3.070	North Spirit Lake Greenstone Belt	Northwest Ontario, Canada	Nesbitt et al., <i>Precambrian Res.</i> 174 , 16-34 (2009).
3.250	Fig Tree Group	Swaziland Supergroup, South Africa	Hofmann, A., <i>Precambrian Res.</i> 143 , 23-49 (2005).
3.400	Geogre Creek Group, Mullagine Area	Western Australia	McLennan et al., <i>Precambrian Res.</i> 22 , 93-124 (1983).

Supplementary Table S3 Additional new data used for the compilation of the secular trends of Mo, Mo/TOC, V, and V/TOC (Figure 3)

Age (Ga)	Formation	Location	Samples	TOC	Fe _{HR} /Fe _T	Fe _{pyrite} /Fe _{HR}	DOP	Mo	V
0.64	Black River Dolomite	Forest-1 Core, Australia and Tasmania	RC06-FOR01-A - 835.84-835.87 m	5.1	1.03	0.94		13.9	194
0.64	Black River Dolomite	Forest-1 Core, Australia and Tasmania	RC06-FOR01-B - 835.77-835.79 m	5.6	0.99	0.95		14.1	197
0.64	Black River Dolomite	Forest-1 Core, Australia and Tasmania	RC06-FOR01-C - 835.70-835.72 m	5.3	1.11	0.96		13.9	204
0.64	Black River Dolomite	Forest-1 Core, Australia and Tasmania	RC06-FOR01-D - 835.65-835.68 m	5.6	0.98	0.95		12.4	195
0.64	Black River Dolomite	Forest-1 Core, Australia and Tasmania	RC06-FOR01-E - 835.58-835.62 m	5.3	1.02	0.95		12.0	196
0.64	Black River Dolomite	Forest-1 Core, Australia and Tasmania	RC06-FOR02-B - 828.11-828.15 m	6.5	0.79	0.93		29.2	321
0.64	Black River Dolomite	Forest-1 Core, Australia and Tasmania	RC06-FOR02-D - 828.23-828.27 m	6.6	0.80	0.93		28.9	327
0.64	Black River Dolomite	Forest-1 Core, Australia and Tasmania	RC06-FOR02-G - 828.37-828.40 m	6.5	0.80	0.93		32.9	367
0.64	Black River Dolomite	Forest-1 Core, Australia and Tasmania	RC06-FOR02-H - 828.48-828.50 m	6.4	0.90	0.93		30.2	345
0.64	Black River Dolomite	Forest-1 Core, Australia and Tasmania	RC06-FOR02-I - 828.55 - 828.58 m	6.8	0.81	0.90		28.8	349
2.05	Zaonezhskaya Fm., Ludikovian Series	Karelia, Russia	C-5190-83	9.3			0.5	7	128
2.05	Zaonezhskaya Fm., Ludikovian Series	Karelia, Russia	C34-64.8	10.2			0.9	74	1954
2.05	Zaonezhskaya Fm., Ludikovian Series	Karelia, Russia	C34-90.7	0.4			0.9	4	70
2.05	Zaonezhskaya Fm., Ludikovian Series	Karelia, Russia	C34-96.5	1.8			0.8	28	1296
2.1	Sengoma Argillite Formation, Pretoria Series	Lobatse, Botswana	171.5	10			0.8	1.6	88
2.1	Sengoma Argillite Formation, Pretoria Series	Lobatse, Botswana	186.57	11			0.7	48.9	1198
2.1	Sengoma Argillite Formation, Pretoria Series	Lobatse, Botswana	200.7	13.3			0.9	10.0	128
2.1	Sengoma Argillite Formation, Pretoria Series	Lobatse, Botswana	202.5	15.5			0.9	6.8	159
2.1	Sengoma Argillite Formation, Pretoria Series	Lobatse, Botswana	205.25	14.2			0.9	26.3	160
2.1	Sengoma Argillite Formation, Pretoria Series	Lobatse, Botswana	209	15.9			0.8	7.4	133
2.1	Sengoma Argillite Formation, Pretoria Series	Lobatse, Botswana	212.7	16			0.7	8.0	112
2.53	Gamhaan Formation	South Africa	WB-98507.39	3			0.5	2.9	21
2.62	Jeerinah Formation, Fortescue Group	WA, Australia	FVG-1 707.95	10.4			0.9	5	110
2.62	Jeerinah Formation, Fortescue Group	WA, Australia	FVG-1752.65	6			0.8	2	98
2.62	Jeerinah Formation, Fortescue Group	WA, Australia	FVG-1765.8	9.9			0.7	2	53
2.62	Jeerinah Formation, Fortescue Group	WA, Australia	FVG-1774	4.4			0.9	3	73
2.62	Jeerinah Formation, Fortescue Group	WA, Australia	FVG-1794.1	4.7			0.7	4	95